



Cite this: *Phys. Chem. Chem. Phys.*,
2018, 20, 12543

Tracking the energy flow in the hydrogen exchange reaction $\text{OH} + \text{H}_2\text{O} \rightarrow \text{H}_2\text{O} + \text{OH}$

Yongfa Zhu,^{id ab} Leilei Ping,^{ac} Mengna Bai,^d Yang Liu,^d Hongwei Song,^{id *a}
Jun Li^{id *d} and Minghui Yang^{id a}

The prototypical hydrogen exchange reaction $\text{OH} + \text{H}_2\text{O} \rightarrow \text{H}_2\text{O} + \text{OH}$ has attracted considerable interest due to its importance in a wide range of chemically active environments. In this work, an accurate global potential energy surface (PES) for the ground electronic state was developed based on $\sim 44\,000$ *ab initio* points at the level of UCCSD(T)-F12a/aug-cc-pVTZ. The PES was fitted using the fundamental invariant-neural network method with a root mean squared error of 4.37 meV. The mode specific dynamics was then studied by the quasi-classical trajectory method on the PES. Furthermore, the normal mode analysis approach was employed to calculate the final vibrational state distribution of the product H_2O , in which a new scheme to acquire the Cartesian coordinates and momenta of each atom in the product molecule from the trajectories was proposed. It was found that, on one hand, excitation of either the symmetric stretching mode or the asymmetric stretching mode of the reactant H_2O promotes the reaction more than the translational energy, which can be rationalized by the sudden vector projection model. On the other hand, the relatively higher efficacy of exciting the symmetric stretching mode than that of the asymmetric stretching mode is caused by the prevalence of the indirect mechanism at low collision energies and the stripping mechanism at high collision energies. In addition, the initial collision energy turns ineffectively into the vibrational energy of the products H_2O and OH while a fraction of the energy transforms into the rotational energy of the product H_2O . Fundamental excitation of the stretching modes of H_2O results in the product H_2O having the highest population in the fundamental state of the asymmetric stretching mode, followed by the ground state and the fundamental state of the symmetric stretching mode.

Received 9th February 2018,
Accepted 4th April 2018

DOI: 10.1039/c8cp00938d

rsc.li/pccp

1. Introduction

Chemical changes are usually accompanied by a redistribution of energy. Whether or not a reaction will be able to proceed depends upon the flow of energy, *viz.*, to what extent can the energy of an excited reactant mode flow into the reaction coordinate at the transition state to promote the reaction.^{1–6} Based on a systematic study of a considerable number of atom–diatom reactions, Polanyi proposed some intuitive and useful rules concerning the relative efficacy of the translational and vibrational excitations in promoting such reactions.⁷ For substantially exothermic reactions in which the barrier is located in the entrance valley (“early barrier”), the favored

degree of freedom would be translation, whereas the reactant vibration would be more effective for substantially endothermic reactions in which the barrier is located in the exit valley (“late barrier”). Taking advantage of the microscopic reversibility, the Polanyi rules can also be used to predict the product energy disposal in reactions. However, when the target reaction presents a central barrier, the Polanyi rules would lose efficacy.

The recently proposed sudden vector projection (SVP) model generalizes the venerable Polanyi rules.⁴ Instead of using the location of the barrier as a descriptor to predict the reactant mode selectivity, the SVP model attributes the efficacy of a reactant mode, translational, vibrational or rotational, in enhancing a reaction to its coupling with the reaction coordinate at the transition state. Although the SVP model has been successfully applied to many polyatomic reactions in the gas phase and at gas-surface interfaces, it has seldom been validated in polyatomic reactions with central barriers.^{8–13} The thermoneutral identity hydrogen abstraction reaction, $\text{OH} + \text{H}_2\text{O} \rightarrow \text{H}_2\text{O} + \text{OH}$, serves as an excellent candidate to test the applicability of the SVP model to central barrier reactions.

The reaction $\text{OH} + \text{H}_2\text{O} \rightarrow \text{H}_2\text{O} + \text{OH}$, which involves the open-shell hydroxyl radical and the breaking and formation of

^a State Key Laboratory of Magnetic Resonance and Atomic and Molecular Physics, Wuhan Institute of Physics and Mathematics, Chinese Academy of Sciences, Wuhan 430071, China. E-mail: hwsong@wipm.ac.cn

^b University of Chinese Academy of Sciences, Beijing 100049, China

^c College of Physical Science and Technology, Huazhong Normal University, Wuhan 430079, China

^d School of Chemistry and Chemical Engineering, Chongqing University, Chongqing 401331, China. E-mail: jli15@cqu.edu.cn

strong covalent bonds, plays an important role in combustion chemistry, organic chemistry, environmental chemistry, atmospheric chemistry, interstellar chemistry and a wide range of other chemically active environments.^{14–29} Due to the symmetry of the reaction, it is impracticable to measure its rate. Dubey *et al.*¹⁷ reported pressure-independent rate constants of $(2.2 \pm 1.0) \times 10^{-16}$, $(3 \pm 1.0) \times 10^{-16}$ and 5×10^{-17} cm³ molecule⁻¹ s⁻¹ at 300 K by substituting the reactant OH with OH¹⁸ and OD and H₂O with D₂O. The significantly lower pre-exponential factor of $A = (2.3 \pm 1.0) \times 10^{-13}$ cm³ molecule⁻¹ s⁻¹ of the reaction OH¹⁸ + H₂O → HOH¹⁸ + OH in the temperature range from 300 to 420 K, as compared with the typical values, was attributed to the formation of a hydrogen-bonded prereaction complex, leading to an entropic constraint. McCabe *et al.*²⁷ measured the rate coefficients for the vibrational relaxation of OH ($\nu = 1$) and OD ($\nu = 1$) by H₂O and D₂O at temperatures from 251 to 390 K and proposed that relaxation involves the transient formation of hydrogen-bonded complexes which can undergo intramolecular vibrational redistribution at a rate competitive with their re-dissociation. On the other hand, theoretical simulations presented consistent results with experimental kinetic data and demonstrated that the tunneling effects are very important especially at low temperatures.^{18,19,30,31} In sharp contrast, dynamics studies were rarely reported for the OH + H₂O → H₂O + OH reaction.^{32,33} Arnold *et al.*¹⁶ and Deyerl *et al.*³⁴ investigated the dynamics in the transition state region of the reaction by photoelectron spectroscopy and photoelectron-photofragment coincidence spectroscopy of the H₃O₂⁻ negative ion. A vibrational progression was observed, indicating excitation of the antisymmetric stretching mode of the product H₂O.

Much theoretical and experimental attention has also been paid to studying the mutual interaction of OH and H₂O.^{20,24,35–55} Experimental infrared spectroscopy in solid Ar matrices,^{20,37,38} in solid Ne matrices⁴⁸ and in liquid helium droplets,^{49,54} and microwave spectroscopy in the gas phase⁴⁰ supported the fact the global minimum of the OH–H₂O complex is a structure with C_s symmetry for which hydrogen bonding occurs between the hydrogen of the hydroxyl radical and the oxygen of water. Theoretical calculations identified two different minima.^{30,36} Besides the aforementioned global minimum, another local minimum was located in which the hydrogen bond occurs between the water H atom and the O atom of the OH radical. Schaefer *et al.*⁵⁵ investigated the stationary points along the reaction path of the OH + H₂O reaction using the “gold standard” coupled cluster method with the singles, doubles, and perturbative triples excitations (CCSD(T)) method with the correlation-consistent basis sets up to the augmented correlation-consistent polarized quintuple zeta basis set (aug-cc-pV5Z, or AV5Z). The global (CP1) and local (CP2) minima are predicted to lie 5.74 and 3.51 kcal mol⁻¹ below the separated reactants, respectively. The transition state (TS1) between CP1 and CP2 has a geometry very close to CP2 and the energy difference between TS1 and CP2 is less than 0.1 kcal mol⁻¹. The classical barrier height for the reaction (TS2) is predicted to be 9.45 kcal mol⁻¹. Very recently, Bai *et al.*³³ constructed an accurate *ab initio*-based potential energy surface (PES) of the reaction by using the

permutation invariant polynomial-neural network method, for which ~48 000 data points are sampled and calculated at the level of CCSD(T)-F12a/aug-cc-pVTZ, resulting in a root mean squared error (RMSE) of 0.12 kcal mol⁻¹.

In this work, a new global, full-dimensional ground-state PES for the OH + H₂O → H₂O + OH reaction is developed using the fundamental-invariant neural network (FI-NN) method⁵⁶ based on ~44 000 *ab initio* points sampled in the relevant configurational space. The energies of the data points are calculated at the level of the explicitly correlated version of the unrestricted CCSD(T)-F12a/AVTZ.^{57,58} The quasi-classical trajectory (QCT) method^{59,60} is then employed to study the dynamics of the reaction, including mode specificity and final-state distribution. In this regard, a new scheme is proposed to extract the final-state information from the trajectories. We aim at understanding the mode-specific dynamics of central barrier reactions and the underlying energy flow in the reaction processes. The paper is organized as follows. Section II outlines the details of the *ab initio* calculations and PES fitting. The quasi-classical trajectory method is given in Section III. This is followed by the results and discussions in Section IV. Finally, the conclusions are supplied in Section V.

II. Potential energy surface

The energies of the *ab initio* points are calculated at the level of FC-UCCSD(T)-F12a/AVTZ, implemented by MOLPRO 2012.1.⁶¹ FC denotes “frozen-core” treatment in the post-Hartree–Fock calculations. The UCCSD(T)-F12 method has been shown to yield atomization energies, electron affinities, ionization potentials, equilibrium geometries and harmonic frequencies for both close and open-shell systems better than the conventional CCSD(T) with the AV5Z basis set, and thus has been widely employed in *ab initio* calculations.^{57,58,62–64}

Sampling *ab initio* points is vital in developing an accurate global PES with reasonable computational cost. In this regard, Atom Centered Density Matrix Propagation (ADMP) molecular dynamics is first employed to sample the relevant configurations using spin-unrestricted Hartree–Fock with the contracted Gaussian basis set 6-311G (UHF/6-311G) by Gaussian 09.⁶⁵ These points are used to generate a raw PES, which is validated by comparing its key properties of stationary points, such as geometry, energy and frequency, with *ab initio* calculations. Starting from the raw PES, batches of trajectories at various energies are dispatched to search for unphysical regions of the PES resulting from the lack of *ab initio* data points in the ADMP sampling. New points that are not close to the existing data set are then added to patch up these unphysical regions. The closeness between a new point $\{\vec{r}_i\}$ and one in the existing data sets $\{\vec{r}'_i\}$ is judged by the Euclidean distance defined in terms of

their bond lengths, $\chi(\vec{r}_i) = \sqrt{\sum_{i=1}^{10} |\vec{r}_i - \vec{r}'_i|^2}$. The new points with $\chi > 0.08$ Å (or 0.1 Å in the asymptotic region) is retained and the permutation equivalent points are also included in such a screening. The procedure is iterated and finally a total of

44 305 points with an energy below 60.0 kcal mol⁻¹ relative to the global minimum are included in the dataset.

The FI-NN method⁵⁶ is employed to fit the PES, in which the permutation invariant of the PES is introduced to the neural network by using fundamental invariants as the input vector. The FI-NN method shares the same spirit as the permutation invariant polynomial neural network (PIP-NN) approach^{66–68} in enforcing the permutation invariant. Instead of using all the PIPs truncated by a given degree as the input vector, FI minimizes the size of the input polynomials. The Morse-like variables, $P_{ij} = \exp(-r_{ij}/\alpha)$, are used to construct the polynomials with α as an adjustable constant ($\alpha = 2.0$ Å) and r_{ij} is the internuclear distance between the i th and j th atoms.^{69,70} For the A₃B₂ molecules, there exist in total 26 fundamental invariants with a maximum degree of 6.

In each NN fitting, the dataset is divided randomly into two sets, namely the training (95%) and validation (5%) sets. The training data is then fitted by the backward propagation neural network with the Levenberg–Marquardt algorithm.⁷¹ The “early stopping” method is used to avoid overfitting.⁷² To avoid false extrapolation due to the edge points in the randomly selected validation set, only fits with a similar RMSE for both sets are accepted. The RMSE is

calculated by $\text{RMSE} = \sqrt{\sum_{i=1}^{N_{\text{data}}} (E_{\text{fit}} - E_{\text{ab initio}})^2 / N_{\text{data}}}$. Besides, the

maximum deviation is also considered in choosing the final PESs. The final PES is taken as the average of several chosen fits, as suggested by the NN ensemble approach to minimize random errors.⁷³ The architecture of the neural network employed is 26-30-70-1, which contains 26 invariant polynomials as inputs, 30 and 70 neurons in two hidden layers, and 1 output of potential energy, resulting in 3051 parameters. Finally, four fits are determined with the RMSEs of the training/validation sets and the maximum deviation being 4.05/9.24/101.08, 4.13/9.20/139.68, 4.14/11.27/145.68, 7.25/15.21/145.35 meV, respectively. The overall RMSE of the averaged PES is 4.37 meV.

III. Quasi-classical trajectory method

Standard QCT calculations, implemented by the software VENUS,⁵⁹ are carried out on the FI-NN PES. The integral cross section (ICS) is calculated by

$$\sigma_{\text{r}}(E_{\text{c}}) = \pi b_{\text{max}}^2 P_{\text{r}}(E_{\text{c}}), \quad (1)$$

where the reaction probability $P_{\text{r}}(E_{\text{c}})$ is defined as the ratio between the numbers of the reactive (N_{r}) and total (N_{tot}) trajectories at a specified collision energy E_{c} . The maximal impact parameter b_{max} is determined using small batches of trajectories with trial values at each specified initial state. The impact parameter b is sampled by $b = R^{1/2} b_{\text{max}}$, where R is a uniform random number in [0,1]. The statistical error is given by $\Delta = \sqrt{(N_{\text{tot}} - N_{\text{r}}) / N_{\text{tot}} N_{\text{r}}}$.

The differential cross section (DCS) is computed by

$$\frac{d\sigma_{\text{r}}}{d\Omega} = \frac{\sigma_{\text{r}} P_{\text{r}}(\theta)}{2\pi \sin(\theta)}, \quad (2)$$

where $P_{\text{r}}(\theta)$ is the normalized probability with the scattering angle θ given by

$$\theta = \cos^{-1} \left(\frac{\vec{v}_i \cdot \vec{v}_f}{|\vec{v}_i| |\vec{v}_f|} \right). \quad (3)$$

Here, $\vec{v}_i = \vec{v}_{\text{OH}} - \vec{v}_{\text{H}_2\text{O}}$ and $\vec{v}_f = \vec{v}_{\text{H}_2\text{O}} - \vec{v}_{\text{OH}}$ denote the initial and final relative velocities. Hence, trajectories with $\theta = 0^\circ$ (180°) correspond to the forward (backward) scattering.

For a diatomic product molecule, the rotational quantum number is determined by the diatom’s rotational angular momentum while the vibrational quantum number is determined by Einstein–Brillouin–Keller semiclassical quantization of the action integral. For the polyatomic product molecule, the normal mode analysis (NMA) approach recently developed by Corchado and Espinosa-Garcia^{74–78} is adopted to assign quantum-like vibrational states. The NMA approach generally yields similar results to the fast Fourier transformation method,^{79,80} but with a lower computational cost. Considering a polyatomic product molecule with N nuclei, the final Cartesian coordinates \vec{r}_i and momenta \vec{p}_i ($i = 1, \dots, N$) in the center of the mass (COM) frame can be obtained directly from the trajectory of VENUS. The angular velocity is calculated by $\vec{\omega}_i = \vec{I}_i^{-1} \vec{L}_i$, in which $\vec{I}_i = m_i \vec{r}_i^2$ is the moment of inertia tensor (m_i denotes the mass of the i th atom) and $\vec{L}_i = \vec{r}_i \times \vec{p}_i$ the angular momentum. To proceed with the normal mode analysis, the angular velocity is removed by

$$\vec{v}_i^{\text{nr}} = \vec{v}_i - \vec{\omega}_i \times \vec{r}_i. \quad (4)$$

In order to project the Cartesian coordinate \vec{r}_i and velocity \vec{v}_i^{nr} on the normal mode space, the displacement of each atom with respect to the reference geometry \vec{r}_i^{ref} must be determined. Thus, the Cartesian coordinates $\{\vec{r}_i\}$ have to be displaced and rotated to make the COM of the molecule coincide with the COM of the reference geometry and the orientation of the molecule approach as much as possible the orientation of the reference geometry. The scheme employed here is the same as that proposed by Corchado and Espinosa-Garcia,⁷⁸ for which a quaternion q is determined by minimizing the function D , defined as

$$D = |q^{\text{T}} r q - r^{\text{ref}}|^2, \quad (5)$$

so that the geometry and momenta are oriented towards the normal modes. Then, the Cartesian coordinate \vec{r}_i and velocity \vec{v}_i^{nr} are rotated as follows:

$$\begin{aligned} \vec{r}_i^{\text{R}} &= q^{\text{T}} \vec{r}_i q \\ \vec{v}_i^{\text{R}} &= q^{\text{T}} \vec{v}_i^{\text{nr}} q \end{aligned}, \quad i = 1, \dots, N. \quad (6)$$

The normal coordinate Q_k and momentum P_k ($k = 1, \dots, 3N - 6$) are calculated by

$$\begin{aligned} Q_k &= \sum_{i=1}^N \sqrt{m_i} \vec{I}_{ki} \Delta \vec{r}_i^{\text{R}} \\ P_k &= \sum_{i=1}^N \sqrt{m_i} \vec{I}_{ki} \vec{v}_i^{\text{R}} \end{aligned}, \quad k = 1, \dots, 3N - 6, \quad (7)$$

where $\Delta \vec{r}_i^{\text{R}} = \vec{r}_i^{\text{R}} - \vec{r}_i^{\text{ref}}$ is the displacement with respect to the reference geometry \vec{r}_i^{ref} in the normal mode space and \vec{I} is the orthogonal transformation matrix that transforms from

mass-scaled Cartesian coordinates to normal coordinates. The matrix \bar{I} and simultaneously the frequency of each mode ω_k are obtained by performing a normal mode analysis of the relevant reference geometry.

The vibrational energy for each normal mode is computed by

$$E_k = T_k + V_k = \frac{P_k^2}{2} + \frac{\omega_k^2 Q_k^2}{2}, \quad k = 1, \dots, 3N - 6, \quad (8)$$

and a noninteger classical harmonic action number for each mode is then obtained as

$$n_k' = \frac{E_k}{\omega_k} - \frac{1}{2}, \quad k = 1, \dots, 3N - 6. \quad (9)$$

This noninteger number needs to be quantized by rounding n_k' to the nearest integer value n_k . It is noteworthy that the NMA approach introduces two approximations: the decoupling of the vibrational and rotational motions and the harmonic approximation. Therefore, this approach may not work well for highly excited product states.

Two binning methods, namely histogram binning (HB)⁸¹ and Gaussian binning (GB),^{77,82} are implemented to confer a “quantum spirit” to these noninteger classical harmonic action numbers. For the HB method, all the trajectories are taken into account in the statistic and each action number is rounded to the nearest integer. The probability of the state \mathbf{n} (\mathbf{n} denotes a vibrational state of the product molecule ($n_1, n_2, \dots, n_{3N-6}$)) is given by

$$P_{\text{HB}}(\mathbf{n}) = \frac{N(\mathbf{n})}{N_{\text{traj}}}. \quad (10)$$

A well-known issue with the HB method is that some product molecules in the QCT calculations present vibrational energies below their zero-point energy. This problem can be partly handled by the GB method, in which a Gaussian weight is calculated for each product. The 1 GB method proposed by Czakó and Bowman⁷⁷ is implemented in this work. The Gaussian weight of the p th product geometry in a given vibrational state \mathbf{n} is calculated by⁷⁷

$$G_p(\mathbf{n}) = \frac{\beta}{\sqrt{\pi}} e^{-\beta^2 ([E(\mathbf{n}_p') - E(\mathbf{n})] / [2E(0)])^2}, \quad p = 1, 2, \dots, N(\mathbf{n}) \quad (11)$$

where $\beta = 2\sqrt{\ln 2}/\delta$ is a positive real parameter and δ is the full width at half maximum. $E(0)$ is the harmonic zero-point energy and $E(\mathbf{n}_p') = \sum_{k=1}^{3N-6} \omega_k \left(n_{k,p}' + \frac{1}{2} \right)$ is the vibrational energy of the p th product geometry and $E(\mathbf{n}) = \sum_{k=1}^{3N-6} \omega_k \left(n_k + \frac{1}{2} \right)$ is the vibrational energy of the state \mathbf{n} assigned using the HB method. The probability is given by

$$P_{\text{GB}}(\mathbf{n}) = \frac{\sum_{p=1}^{N(\mathbf{n})} G_p(\mathbf{n})}{N_{\text{traj}}}. \quad (12)$$

The start point to perform NMA calculations is to acquire the Cartesian coordinates and momenta of each atom in the

product molecule from the trajectories. Traditionally, these quantities are taken from the last step of the trajectory, denoted as Method 1. However, due to the inherent defect of the harmonic approximation, a large error of the calculated potential energy V_k would be expected when the geometry extracted from the trajectory deviates visibly from the reference geometry, resulting in an unphysical action number. A crude, but easy way to overcome the problem is to average action numbers over at least one molecular vibration period from each trajectory, denoted as Method 2, so that the error is supposed to be canceled out. In this work, the Cartesian coordinates and momenta are extracted from one step of each reactive trajectory within the last vibrational period of the product molecule, denoted as Method 3. This step is determined by demanding that the corresponding geometry has the minimum potential energy V_k within the vibrational period. This constraint is physically reasonable because a geometry presenting the smallest potential energy within one vibrational period resembles most the reference geometry. A comparison has been made on the accuracies of Method 1, Method 2 and Method 3, for which thousands of trajectories are launched from the reactant asymptotic region with a well-defined initial state, followed immediately by NMA calculations. The three aforementioned methods are implemented to extract the state distributions of the reactants. The obtained results are then compared with the initially defined state distribution. It is concluded that the third method generally yields relatively more accurate results although the three methods are all qualitatively correct. We are now testing the different NMA methods in more systems, including tetra-atomic reactions, penta-atomic reactions and hexa-atomic reactions with early, central and late barriers. Details will be given in a subsequent paper, in which different 1 GB methods^{77,83,84} will be compared as well.

Batches of trajectories (200 000–800 000) are run with collision energies ranging from 6 kcal mol⁻¹ to 30 kcal mol⁻¹.

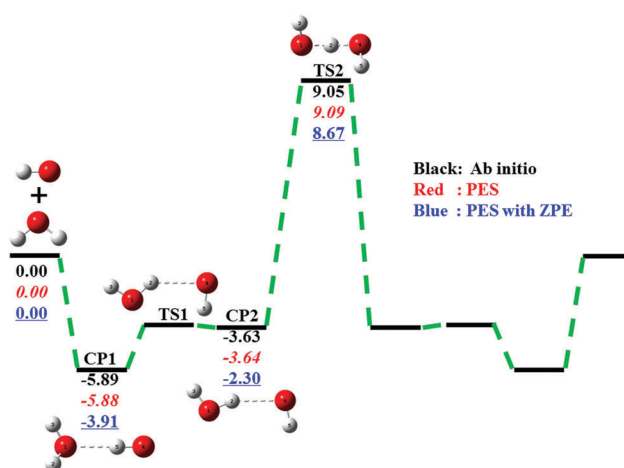


Fig. 1 Schematic illustration of the reaction path for the $\text{OH} + \text{H}_2\text{O} \rightarrow \text{H}_2\text{O} + \text{OH}$ reaction. The *ab initio* energies of the stationary points at the level of UCCSD(T)/AVTZ, the values of the fitted PES (italic) and the ZPE corrected values (underlined) are shown below the corresponding geometries. All energies are given in kcal mol⁻¹ and relative to the reactant asymptote.

The statistical errors are all below 5% except for the 8 kcal mol⁻¹ from the reactant ground state. The initial vibrational states of H₂O are sampled using the fixed normal mode method while the initial states of OH are sampled using the conventional semi-classical method. The trajectories are initiated with a reactant separation of 9.0 Å, and terminated when the products or reactants reach a separation of 10.0 Å for reactive or non-reactive trajectories. The gradient of the PES is obtained numerically by a central difference algorithm. The time step is

selected to be 0.05 fs, which converses the energy better than 10⁻³ kcal mol⁻¹ in the propagation.

IV. Results and discussion

A. Properties of potential energy surface

Fig. 1 shows a schematic diagram of the reaction path for the OH + H₂O → H₂O + OH reaction. The minimum energy path is

Table 1 Geometries in the internal coordinates (length in angstrom and angle in degree) of the stationary points for the OH + H₂O → H₂O + OH reaction. The corresponding atom labels are shown in Fig. 1

Species	Method	$R_{O_1H_2}$	$R_{O_1H_3}$	$R_{H_2O_4}$	$R_{O_1H_5}$	$\theta_{H_2O_1H_3}$	$\theta_{O_1H_2O_4}$	$\theta_{H_2O_4H_5}$	$\varphi_{H_3O_4H_2O_1}$	$\varphi_{O_1H_2O_1H_3}$
OH	<i>Ab initio</i> ^a				0.973					
	PES ^b				0.970					
	Expt. ^c				0.970					
H ₂ O	<i>Ab initio</i> ^a	0.962				104.15				
	PES ^b	0.958				104.52				
	Expt. ^c	0.958				104.48				
CP1	<i>Ab initio</i> ^a	0.962	0.962	3.461	0.979	104.99	48.83	14.69	-4.87	-136.70
	PES ^b	0.959	0.959	3.469	0.976	105.17	45.77	14.84	-8.32	-140.18
TS1	<i>Ab initio</i> ^a	0.964	0.961	2.150	0.975	105.08	136.27	84.22	0.00	180.00
	PES ^b	—	—	—	—	—	—	—	—	—
CP2	<i>Ab initio</i> ^a	0.965	0.961	2.073	0.975	104.78	157.90	99.75	0.00	180.00
	PES ^b	0.963	0.958	2.078	0.972	105.05	164.37	100.42	0.00	180.00
TS2	<i>Ab initio</i> ^a	1.164	0.970	1.163	0.970	102.72	142.47	102.76	60.28	60.28
	PES ^b	1.165	0.968	1.165	0.968	103.47	141.33	103.47	59.77	59.77

^a This work, UCCSD(T)/AVTZ by Gaussian 09. ^b This work, FI-NN PES. ^c See <http://cccbdb.nist.gov>.

Table 2 Energies (in kcal mol⁻¹) and harmonic frequencies (in cm⁻¹) of the stationary points for the OH + H₂O → H₂O + OH reaction

Frequency (cm ⁻¹)											
Species	Method	E (kcal mol ⁻¹)	1	2	3	4	5	6	7	8	9
OH + H ₂ O	<i>Ab initio</i> ^a	0.00	3719	3920	3812	1645					
	<i>Ab initio</i> ^b	0.00	3738	3942	3832	1647					
	<i>Ab initio</i> ^c	0.00	3742	3943	3833	1649					
	PES ^d	0.00	3744	3943	3832	1646					
	Expt. ^e		3738	3756	3657	1595					
CP1	<i>Ab initio</i> ^a	-5.89	3918	3811	3619	1644	623	423	186	160	149
	<i>Ab initio</i> ^b	-5.89	3939	3831	3632	1646	621	417	189	169	152
	<i>Ab initio</i> ^c	-5.74	3943	3835	3640	1650	614	409	188	161	134
	PES ^d	-5.88	3929	3833	3665	1651	541	409	190	170	162
TS1	<i>Ab initio</i> ^a	-3.63	3908	3785	3699	1644	414	259	158	101	115i
	<i>Ab initio</i> ^c	-3.51	3929	3802	3724	1652	409	261	161	105	73i
	PES ^d										
CP2	<i>Ab initio</i> ^a	-3.68	3901	3775	3707	1655	374	297	160	97	90
	<i>Ab initio</i> ^b	-3.63	3923	3794	3725	1655	386	314	166	149	90
	<i>Ab initio</i> ^c	-3.51	3926	3796	3729	1659	380	289	164	106	72
	PES ^d	-3.64	3934	3789	3736	1650	366	288	159	112	72
CP2-cis	<i>Ab initio</i> ^a	-2.93	3945	3833	3754	1673	329	267	166	126	66i
	<i>Ab initio</i> ^b	-2.90	3924	3803	3735	1661	331	279	165	134	57
	PES ^d	-3.14	3926	3802	3770	1667	347	324	215	152	44i
TS2	<i>Ab initio</i> ^a	9.12	3774	3770	1571	1372	918	577	431	344	1958i
	<i>Ab initio</i> ^b	9.05	3791	3786	1588	1368	922	574	435	359	2244i
	<i>Ab initio</i> ^c	9.45	3797	3792	1588	1362	924	579	438	363	1958i
	PES ^d	9.09	3798	3776	1608	1383	908	574	478	351	2007i

^a This work, UCCSD(T)/AVTZ in Gaussian 09. ^b UCCSD(T)-F12a/AVTZ in Molpro 2015.1, see ref. 33. ^c CCSD(T)/AV5Z, see ref. 55. ^d This work, FI-NN PES. ^e See <http://cccbdb.nist.gov>.

symmetric with respect to the barrier of TS2, featuring two minima (CP1 and CP2) in the entrance valley. The geometries of all the stationary points are optimized at the level of FC-UCCSD(T)/AVTZ, using Gaussian 09, Revision B.01,⁶⁵ which are listed in Table 1 in the internal coordinates. For the reactants OH and H₂O, their geometries in the PES agree well with the *ab initio* calculations with the bond length difference less than 0.004 Å and the angle difference less than 0.4°. The experimental values are also listed for comparison. The conformity of the fitted geometries with experimental values becomes even slightly better than with *ab initio* calculations. For other stationary points but TS1, the fitted geometries also compare well with the *ab initio* values. The fitted bond lengths deviate from the *ab initio* values less than 0.008 Å. Nevertheless, the angle discrepancies of CP1 and CP2 appear to be slightly larger although they are all acceptable for the reaction dynamics calculations. In addition, as mentioned above, TS1 is very close to CP2 with an energy difference smaller than 0.1 kcal mol⁻¹ and, therefore, searching for it in the PES would be in vain.

The energies and harmonic frequencies of the stationary points are calculated at the level of FC-UCCSD(T)/AVTZ and listed in Table 2, together with Bai *et al.*'s results³³ at the level of FC-UCCSD(T)-F12a/AVTZ. The benchmark results reported by Gao *et al.*⁵⁵ at the level of FC-UCCSD(T)/AV5Z are also shown in the same table for comparison. A *cis* form of CP2, denoted by CP2-*cis*, which has a planar geometry and was first reported by Bai *et al.*³³ is also presented. It can be seen that the *ab initio* values at the level of FC-UCCSD(T)/AVTZ and FC-UCCSD(T)-F12a/AVTZ are very close to the benchmark results. The energy difference between FC-UCCSD(T)-F12a/AVTZ and FC-UCCSD(T)/AV5Z is less than 0.4 kcal mol⁻¹ and the frequency difference less than 10 cm⁻¹ except for several torsional modes. As for the transition state of the reaction (TS2), the imaginary frequency predicted by

FC-UCCSD(T)-F12a/AVTZ is 286 cm⁻¹ higher than the benchmark value. The good agreement between the values of FC-UCCSD(T)-F12a/AVTZ and FC-UCCSD(T)/AV5Z indicates that the former method is suitable for the current study. On the other hand, the energies of the stationary points are well reproduced by the PES, typically less than 0.24 kcal mol⁻¹. The frequencies calculated on the PES are in good accord with the *ab initio* values as well. Interestingly, the fitted imaginary frequency of TS2 approaches more the benchmark value although it is 237 cm⁻¹ lower than the *ab initio* value at the level of FC-UCCSD(T)-F12a/AVTZ.

Fig. 2 displays a contour plot of the PES as a function of the bond length of the breaking and forming OH bonds while all the other internal coordinates are optimized. Clearly, the fitted PES is globally smooth and there does not exist any artificial well. The minimum energy path (MEP) associated with the saddle point of TS2 on the PES, as shown in the upper panel of Fig. 3, is determined using the software POLYRATE 9.7,⁸⁵ starting from the saddle point geometry and going downhill to the pre- and post-reaction wells of CP2 in mass-weighted Cartesian coordinates with a step size of 5.0×10^{-5} amu^{1/2} Å. The reaction coordinate (*s*) is defined as the signed distance from the saddle point (*s* = 0), with *s* > 0 referring to the product side and *s* < 0 to the reactant side. The MEP is followed between *s* = -2.0 and *s* = 2.0 amu^{1/2} Å and the Hessian matrix

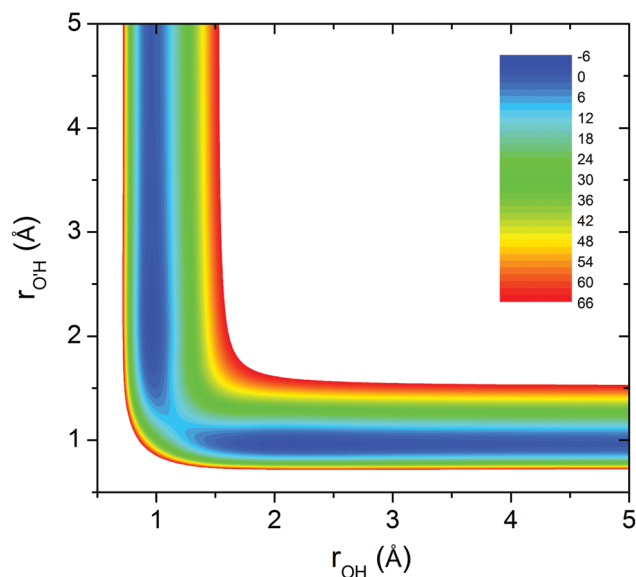


Fig. 2 Contours of the PES as a function of the bond length of the breaking and forming OH bonds with all the other coordinates optimized. The energy is taken from 0 to 66 kcal mol⁻¹ with an interval of 2 kcal mol⁻¹.

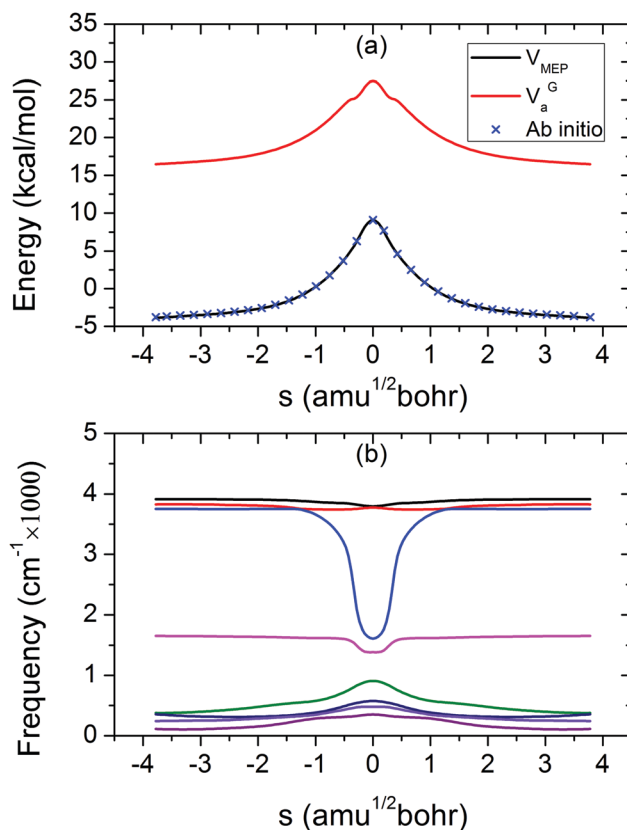


Fig. 3 (a) Minimum energy path, V_{MEP} , and vibrational adiabatic ground state energy, V_a^G , as a function of the reaction coordinate *s*. *Ab initio* energies along the minimum energy path are also given for comparison; (b) generalized normal mode vibrational frequencies as a function of *s*.

is calculated every 9 steps. To validate the accuracy of the fitted PES, *ab initio* calculations along the MEP are also performed. Clearly, the MEP on the PES coincides exactly with the *ab initio* data, suggesting a good description of the reaction path for the PES. Meanwhile, the redundant curvilinear projection formalism is utilized to carry out a generalized normal-mode analysis along the reaction coordinate. The obtained generalized normal mode vibrational frequencies are shown in the lower panel of Fig. 3. The frequency of each mode varies smoothly with the reaction coordinate s . The vibrationally adiabatic ground state energy, defined as $V_a^G(s) = V_{\text{MEP}}(s) + \varepsilon_{\text{int}}(s)$, is displayed in the upper panel as well. $\varepsilon_{\text{int}}(s)$ is one-half the sum of the vibrational frequencies of the generalized normal modes orthogonal to the reaction coordinate at s .

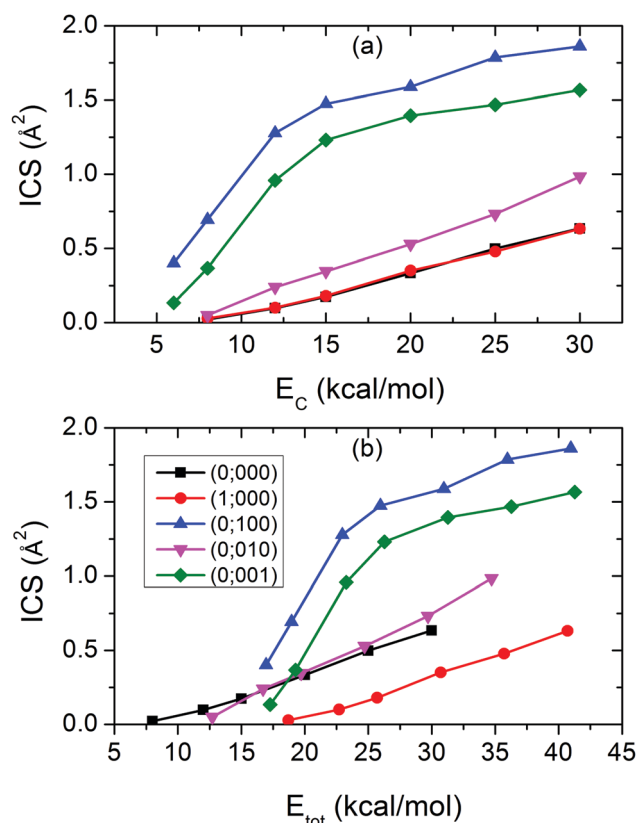


Fig. 4 Integral cross sections of the $\text{OH} + \text{H}_2\text{O} \rightarrow \text{H}_2\text{O} + \text{OH}$ reaction as a function of (a) collision energy and (b) total energy. The numbers (ν_{OH} ; ν_1 , ν_2 , ν_3) in parenthesis denote excitations in the OH vibration, the symmetric stretching mode, the bending mode and the asymmetric stretching mode of H_2O , respectively.

Table 3 SVP values for the $\text{OH} + \text{H}_2\text{O} \rightarrow \text{H}_2\text{O} + \text{OH}$ reaction

Species	SVP
	$\text{OH} + \text{H}_2\text{O} \rightarrow \text{H}_2\text{O} + \text{OH}$
ν_1	0.67
ν_2	0.10
ν_3	0.64
ν_{OH}	0.01
Trans	0.17

B. Mode-specific dynamics

Fig. 4 shows the calculated integral cross sections (ICSs) of the $\text{OH} + \text{H}_2\text{O} \rightarrow \text{H}_2\text{O} + \text{OH}$ reaction from the ground and fundamental states of OH and H_2O . The vibrational states of the reactants OH and H_2O are labeled by $(\nu_{\text{OH}}; \nu_1, \nu_2, \nu_3)$, in which ν_{OH} refers to excitation in the OH vibrational mode and the following three numbers (ν_1, ν_2, ν_3) denote excitations in the symmetric stretching mode, the bending mode, and the anti-symmetric stretching mode, respectively. In Fig. 4(a), the ICSs are plotted as a function of the translational energy. It can be seen that the ICS from each state increases monotonically with the collision energy, satisfying the activation nature of the reaction. Excitation of either the symmetric mode (ν_1) or the asymmetric stretching mode (ν_3) of the reactant H_2O significantly promotes the reaction while excitation of the bending mode (ν_2) presents a slight but visible enhancement effect. It is noteworthy that exciting the symmetric stretching mode is remarkably more efficient than exciting the asymmetric stretching mode in promoting the reaction over the energy region studied. Besides, the excitation energy initially deposited in the OH vibrational mode (ν_{OH}) has a negligible effect on the reaction. The spectator behavior of the OH bond can be easily understood by considering that the bond length of OH varies along the MEP within only 0.005 Å.

The ICSs are depicted in Fig. 4b as a function of the total energy. The total energy is relative to the reactant ground states. Excitation of the symmetric stretching mode (ν_1) possesses the largest reactivity, which is followed by the asymmetric stretching mode (ν_3). They both are more efficient than the translation energy in promoting the reaction except at low collision energies. Excitation of the bending mode (ν_2) has a similar reactivity to the translational energy. The recently proposed SVP model,⁴ which assumes that the reaction occurs in a sudden limit, can provide some physical insights into the mode selectivity. This attributes the efficacy of a reactant mode in promoting the reaction to the projection of its normal vector (\vec{Q}_i) onto the

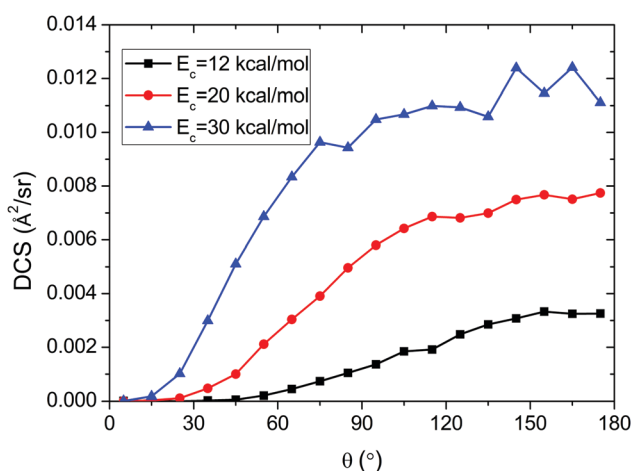


Fig. 5 Differential cross sections of the $\text{OH} + \text{H}_2\text{O} \rightarrow \text{H}_2\text{O} + \text{OH}$ reaction from the ground states of both reactants with the collision energy taken at 12, 20 and 30 kcal mol⁻¹.

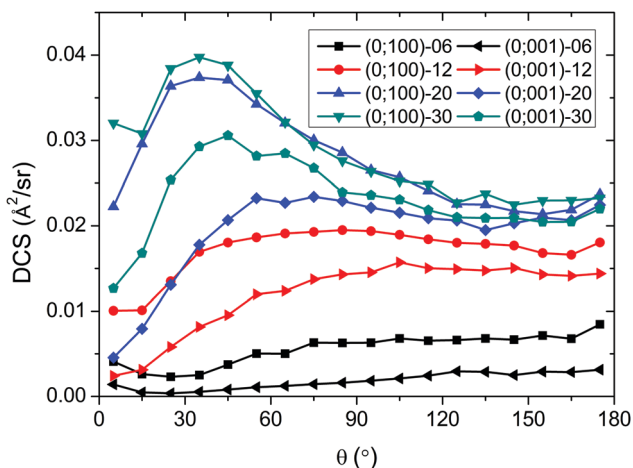


Fig. 6 Differential cross sections of the OH + H₂O → H₂O + OH reaction from the fundamental states of the symmetric and asymmetric stretching modes of H₂O with the collision energy taken at 6, 12, 20, and 30 kcal mol⁻¹.

reaction coordinate vector (\vec{Q}_{RC}) at the transition state: $P_i = \vec{Q}_i \cdot \vec{Q}_{RC} \in [0,1]$. The calculated SVP values are listed in Table 3. The symmetric stretching mode of H₂O has the largest projection ($P_{v_1} = 0.67$), followed by a slightly small value of the asymmetric stretching mode ($P_{v_3} = 0.64$). They are both larger than the projection of the translation mode ($P_{trans} = 0.17$), indicating that excitation in the stretching mode promotes the reaction

more than the translational energy. The vector of the vibrational mode of OH (v_{OH}) has a negligible projection on the reaction coordinate vector, predicting that the OH bond is a good spectator. These predictions agree well with the QCT results. However, the SVP value of the bending mode (v_2) is 0.10, which is smaller than the value of the translational mode, implying that the translation energy is more efficient than the bending mode excitation. This is somewhat different from the QCT calculations. Actually, Guo *et al.*⁴ have pointed out that predictions involving bending modes are not as reliable because of the much lower frequencies at the transition state. In addition, the different efficacies of exciting the two stretching modes observed in the QCT calculations are also not well predicted by the SVP model.

Fig. 5 shows the differential cross sections (DCSs) from the ground states of both reactants. The collision energy is taken at 12, 20 and 30 kcal mol⁻¹. At low collision energies, the reaction prefers backward scattering although the sideways scattering is also significant. As the collision energy increases, the contribution of the sideways scattering becomes comparable to the backward scattering. The preference of the backward scattering indicates that the reaction is mainly dominated by the direct rebound mechanism at low collision energies. Nevertheless, the stripping mechanism becomes increasingly vigorous at high energies. Actually, as has been pointed by Bai *et al.*,³³ the direct rebound mechanism dominates small impact parameter collisions while the stripping mechanism mainly results from large impact parameter collisions.

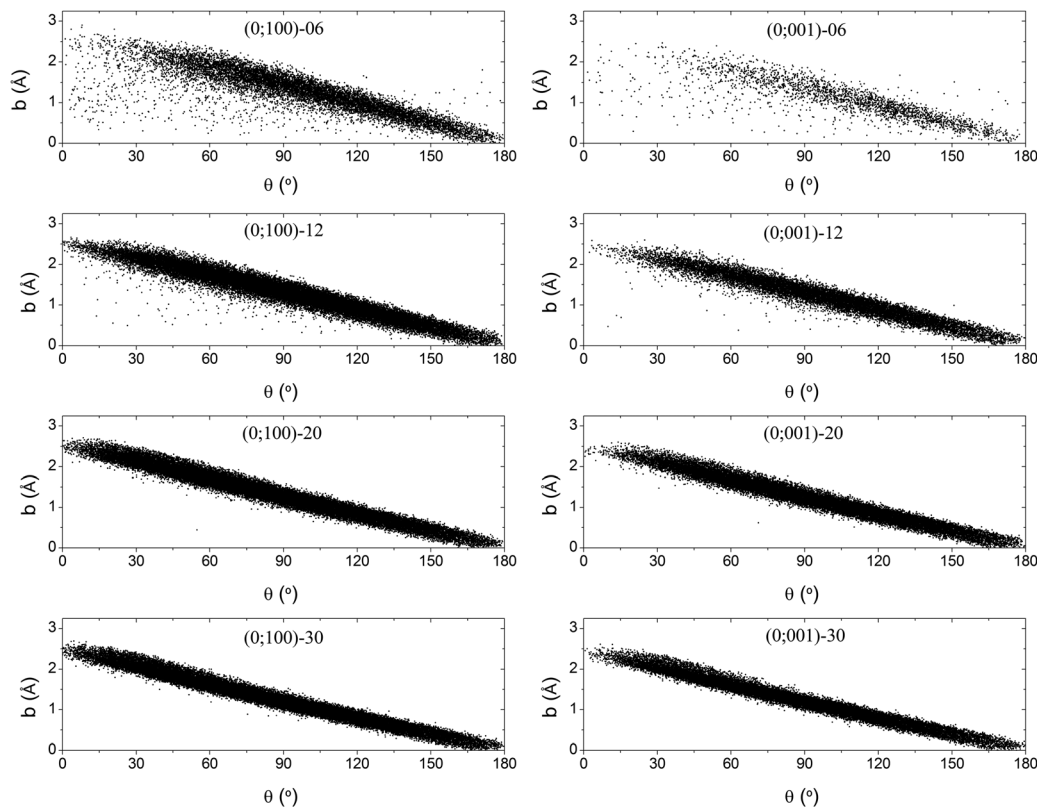


Fig. 7 Correlation between the impact parameter and the scattering angle for the OH + H₂O → H₂O + OH reaction with the reactant H₂O in the fundamental states of the symmetric and asymmetric stretching modes and the collision energies at 6, 12, 20, and 30 kcal mol⁻¹.

The relative efficacy of the symmetric and asymmetric stretching modes of hydride reactants has been debated in the mode-specific dynamics studies of elementary chemical reactions.¹¹ It is thus not trivial to unveil the reaction mechanism resulting in the disparate efficiencies of the two stretching modes of H₂O in promoting the reaction. Fig. 6 shows the DCSs from the fundamental states of the symmetric and asymmetric stretching modes of H₂O with the collision energies taken at 6, 12, 20 and 30 kcal mol⁻¹. Firstly, the product H₂O is almost isotropically scattered at low collision energies, quite different from the distribution from the reactant ground states, at which the reaction favors backward scattering. The isotropic distribution of the product H₂O indicates that the pre- and/or post-reaction wells play an important role in the reaction process when the reactant H₂O is excited to the fundamental states of the symmetric and asymmetric stretching modes. The product angular distribution looks somewhat like the dynamical signature of a complex-forming reaction, for which the product is nearly symmetrically scattered in the forward and backward directions, stemming typically, but not always, from the long lifetime of the reaction intermediate.⁸⁶ Considering the systematically larger reactivity of exciting the symmetric stretching mode (ν_1) than that of exciting the asymmetric stretching mode (ν_3), fundamental excitation of the symmetric stretching mode of H₂O is expected to favor the formation of the hydrogen-bond complex that enhances

the reaction at low collision energies. Secondly, as the collision energy increases, the sideways scattering in the forward hemisphere becomes dominant although the backward scattering is also remarkable. Meanwhile, the DCS of exciting the symmetric stretching mode is significantly larger than the corresponding DCS of exciting the asymmetric stretching mode in the forward hemisphere. Therefore, the discrepancy between the symmetric and asymmetric stretching modes mainly originates from the sideways scattering.

To clarify the underlying reaction mechanisms, the correlation between the impact parameter and the scattering angle is displayed in Fig. 7 with the reactant H₂O in the fundamental states of the symmetric and asymmetric stretching modes and the collision energies at 6, 12, 20, and 30 kcal mol⁻¹. Clearly, the data is more scattered at low collision energies, indicating that there exists another reaction mechanism, the indirect mechanism, in the reaction besides the aforementioned direct rebound and stripping mechanisms because the direct rebound and stripping mechanisms would result in the data points being distributed along the diagonal line. At high collision energies, the scattering in the forward hemisphere is correlated to large impact parameter collisions, thus resulting from the stripping mechanism. Consequently, the larger efficacy of exciting the symmetric stretching mode than exciting the asymmetric stretching mode in promoting the reaction

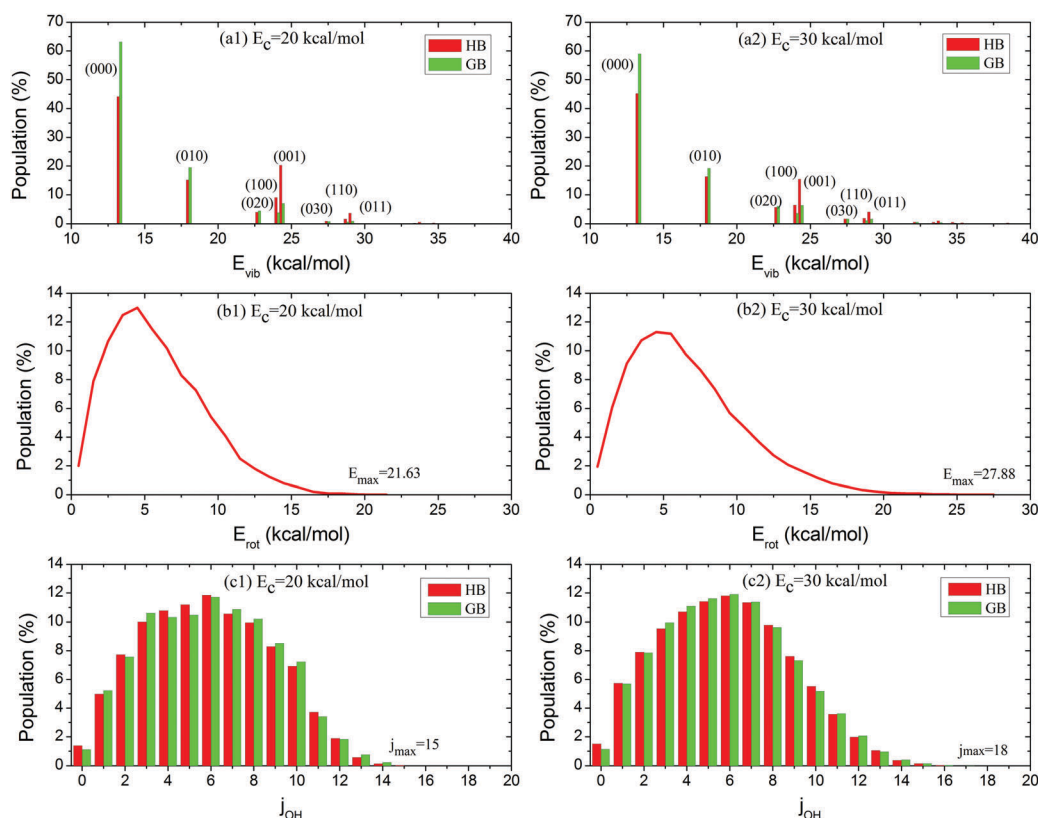


Fig. 8 (a) Vibrational state distributions of the product H₂O, (b) rotational energy distributions of the product H₂O, (c) rotational state distributions of the product OH for the OH + H₂O → H₂O + OH reaction from the reactant ground states at $E_c = 20$ (left, denoted by 1) and 30 (right, denoted by 2) kcal mol⁻¹. The two binning methods HB and GB are color coded as red and green, respectively. The product OH is exclusively in the ground vibrational state and thus not shown here.

is caused by the prevalence of the indirect mechanism at low collision energies and the stripping mechanism at high collision energies. The vibrational energy initially deposited in the symmetric stretching mode promotes the reaction to proceed more *via* the relevant mechanisms at different collision energies than the energy deposited in the asymmetric stretching mode.

C. Final-state distribution

A comprehensive understanding of the microscopic reaction mechanism requires a state-to-state description of the dynamics. This section addresses the question on how the reactant translational and vibrational excitations influence the product energy disposal. The reactants H₂O and OH are both restricted to the ground rotational states in this work. Fig. 8 shows the vibrational state distributions and rotational energy disposal of the product H₂O and the rotational state distributions of the product OH from the reactant ground states with the collision energies fixed at 20 (left) and 30 (right) kcal mol⁻¹. It can be seen from Fig. 8a1 and a2 that the product H₂O is dominant in the ground vibrational state, with slight but visible populations in the fundamental bands of the stretching and/or bending modes, the first and second overtones of the bending mode and the combination bands. The similar pattern of the distributions from the two collision energies means that the initial collision energy cannot flow effectively into the

vibrational modes of the product H₂O. The corresponding rotational energy disposal of H₂O is displayed in Fig. 8b1 and b2. The maximum rotational energy obtained by the product H₂O increases from 21.6 kcal mol⁻¹ to 27.9 kcal mol⁻¹ when the collision rises from 20 kcal mol⁻¹ to 30 kcal mol⁻¹, although the peak value of the rotational energy distribution remains at $E_{\text{rot}} = 4.5$ kcal mol⁻¹. The small increment of the available rotational energy indicates that part of the initial collision energy turns into the rotational energy of H₂O. The product OH is exclusively in the ground vibrational state and thus is not shown in the figure. The rotational state distributions of OH are given in Fig. 8c1 and c2. The two distributions are close to each other, both of which have a maximum population at $j_{\text{OH}} = 6$. Thus, the change of the initial collision energy from 20 to 30 kcal mol⁻¹ has a negligible effect on the final state distribution of OH. It should be noted that the indirect mechanism plays an important role in the low collision energy region, and in this case the initial collision energy is expected to have a remarkable effect on the product energy disposal.

Fig. 9 shows the vibrational state distributions and the rotational energy disposal of the product H₂O from the fundamental states of the symmetric stretching mode and the asymmetric stretching mode of H₂O and the OH vibrational mode with the collision energy fixed at 20 kcal mol⁻¹. For the reactant H₂O in the fundamental state of the symmetric stretching mode and the reactant OH in the ground state, as shown in

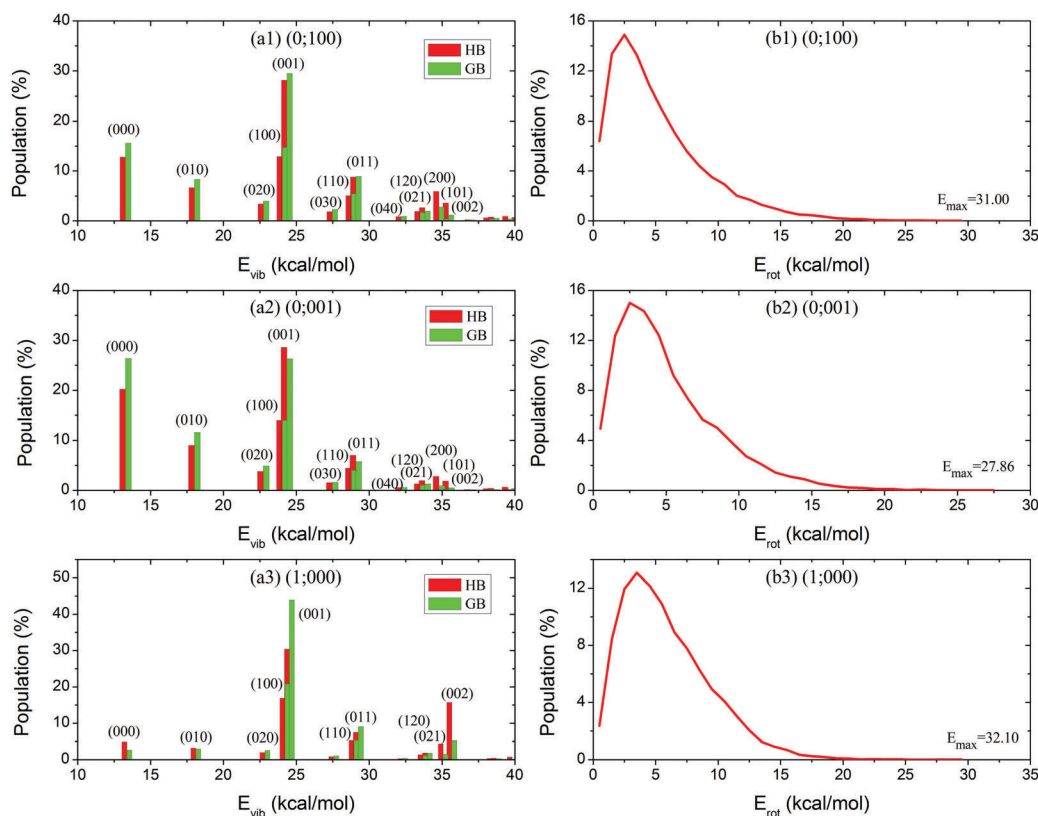


Fig. 9 (a) Vibrational state distributions and (b) rotational energy distributions of the product H₂O for the OH + H₂O → H₂O + OH reaction from the fundamental states of the symmetric stretching mode (upper, labeled by 1) and the asymmetric stretching mode (middle, labeled by 2) of H₂O and the OH vibration mode (lower, labeled by 3) at $E_c = 20$ kcal mol⁻¹. The two binning methods HB and GB are color coded as red and green, respectively.

Fig. 9a1 and b1, the product H₂O is mainly distributed to the fundamental state of the asymmetric stretching mode with a proportion of about 30%, followed by the fundamental state of the symmetric stretching mode and the ground state with an individual proportion of about 15%. The proportions for the other states are relatively small, less than 10% for each one. The corresponding rotational energy distribution has a peak at $E_{\text{rot}} = 2.5 \text{ kcal mol}^{-1}$ and the maximum available rotational energy is $31.0 \text{ kcal mol}^{-1}$. For the reactant H₂O in the fundamental state of the asymmetric stretching mode, as shown in Fig. 9a2 and b2, the product H₂O is largely populated into the fundamental state of the asymmetric stretching mode and the ground state with an individual proportion of about 25%, followed by the fundamental state of the symmetric stretching mode of 15% and the fundamental state of the bending mode of 10%. Note that the proportions obtained by the two binning methods HB and GB are slightly different and the GB method is expected to be more reliable thereafter. The corresponding rotational energy distribution peaks at $E_{\text{rot}} = 2.5 \text{ kcal mol}^{-1}$ and the maximum available rotational energy is $27.9 \text{ kcal mol}^{-1}$. When the reactant OH is excited to the first vibrational state, as shown in Fig. 9a3 and b3, the product H₂O is predominantly distributed to the fundamental state of the asymmetric stretching mode with a proportion of about 45%, followed by the fundamental state of the symmetric stretching mode with a proportion of about 20%. Different from the relatively large

population of the ground state of the product H₂O from the fundamental excitations of the stretching modes of the reactant H₂O, the proportion is less than 5%. The corresponding rotational energy distribution peaks at $E_{\text{rot}} = 3.0 \text{ kcal mol}^{-1}$ and the maximum available rotational energy is $32.1 \text{ kcal mol}^{-1}$.

Fig. 10 presents the vibrational and rotational state distributions of the product OH from the fundamental states of the symmetric stretching mode, the asymmetric stretching mode and the OH vibration mode with the collision energy fixed at 20 kcal mol^{-1} . For the reactant H₂O in the fundamental state of the symmetric stretching mode, about 93% of the product OH is in the ground state and the rest is in the first excited state. When the reactant H₂O is excited to the fundamental state of the asymmetric stretching mode, about 88% of the product OH is in the ground vibrational state. In addition, the product OH is exclusively in the ground vibrational state when the reactant OH is excited to the first vibrationally excited state. The rotational state distributions of the product OH are similar for different initial states. They all have a maximum at $j_{\text{OH}} = 5$ and the maximum accessible rotational state is around 16.

As mentioned in Section IV.B., exciting the symmetric stretching mode promotes the reaction more than exciting the asymmetric stretching mode, which can be partially attributed to the preference of the stripping mechanism at high collision energies. If so, it means that, on one hand, the initial excitation energy deposited in the symmetric stretching mode flows into

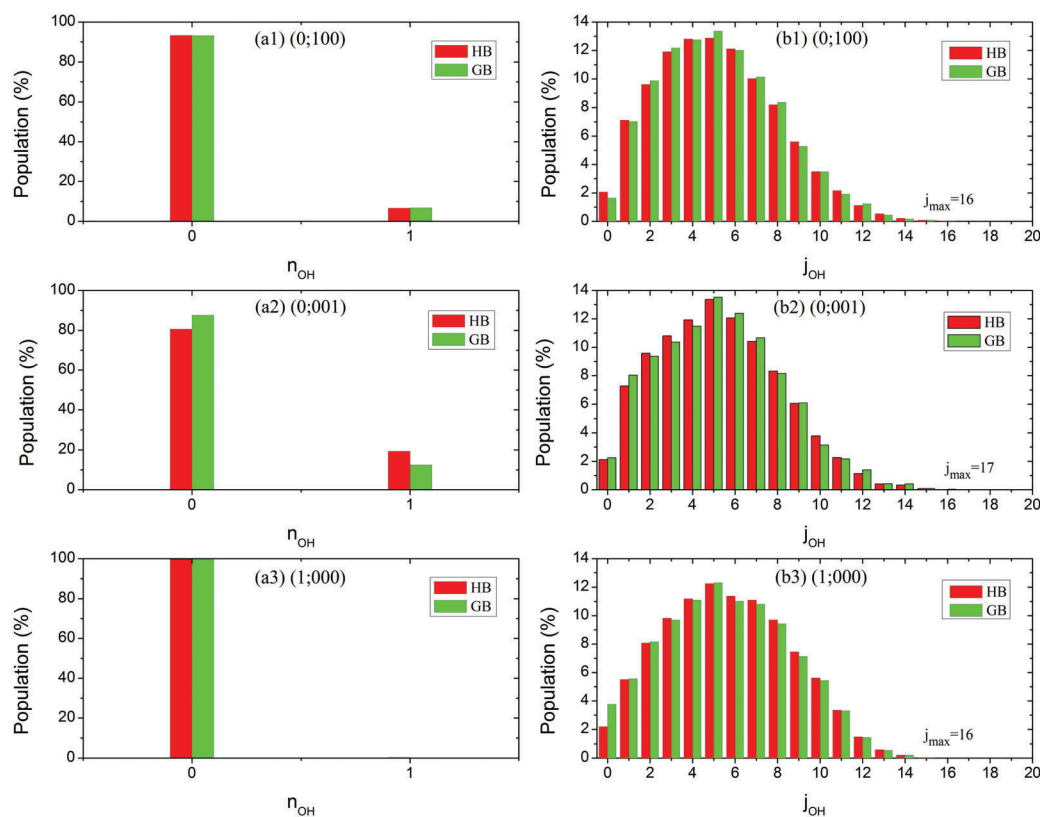


Fig. 10 (a) Vibrational state distributions and (b) rotational state distributions of the product OH for the $\text{OH} + \text{H}_2\text{O} \rightarrow \text{H}_2\text{O} + \text{OH}$ reaction from the fundamental states of the symmetric stretching mode (upper, labeled by 1), the asymmetric stretching mode (middle, labeled by 2) and the OH vibration mode (lower, labeled by 3) at $E_c = 20 \text{ kcal mol}^{-1}$. The two binning methods HB and GB are color coded as red and green, respectively.

the reaction coordinate more efficiently than the excitation energy of the asymmetric stretching mode. On the other hand, the energy flowing into the reaction coordinate will turn into the product kinetic energy *via* the stripping mechanism. Thus, it would be expected that the product OH obtained by exciting the symmetric stretching mode falls into the ground state more. This is actually consistent with the obtained vibrational state distribution of OH.

V. Conclusions

In this work, we report an accurate full-dimensional global PES for the $\text{OH} + \text{H}_2\text{O} \rightarrow \text{H}_2\text{O} + \text{OH}$ reaction based on $\sim 44\,000$ *ab initio* points, whose energies are calculated at the level of UCCSD(T)-F12a/AVTZ. The PES is fitted with a RMSE of 4.37 meV using the FI-NN approach. The reaction path is symmetric with respect to the central barrier and features two hydrogen-bond complexes on both sides. The properties of these stationary points are well reproduced by the PES.

The quasi-classical trajectory method is employed to study the mode-specific dynamics of the $\text{OH} + \text{H}_2\text{O}$ reaction. Excitation of either the symmetric stretching mode or the asymmetric stretching mode of the reactant H_2O notably enhances the reactivity while excitation of the bending mode has a slight enhancement effect. Exciting the symmetric stretching mode shows a visibly higher efficacy than exciting the asymmetric stretching mode in promoting the reaction, which is attributed to the prevalence of the indirect mechanism at low collision energies and the stripping mechanism at high collision energies. In addition, the relatively higher efficiency of the vibrational energy initially deposited in the stretching modes of H_2O than the translational energy is successfully predicted by the SVP model although the efficiency of the bending mode is underestimated.

The final-state distributions are obtained by the normal mode analysis approach in combination with a new scheme to acquire the Cartesian coordinates and momenta of each atom in the product molecule from the trajectories. The initial collision energy cannot flow effectively into the vibrational modes of the products H_2O and OH while a fraction of the energy transforms into the rotational energy of the product H_2O . When the reactant H_2O is fundamentally excited to the symmetric or asymmetric stretching mode, the product H_2O has the highest population in the fundamental state of the asymmetric stretching mode, followed by the ground state and the fundamental states of the symmetric stretching mode. Most of the vibrational energy initially deposited in the spectator bond OH is retained in the OH bond during the reaction process and finally turns into the vibrational energy of the product H_2O . For all the initial states studied in this work, the product OH is dominant in the ground state.

Conflicts of interest

There are no conflicts to declare.

Acknowledgements

This work is supported by the National Natural Science Foundation of China (Grant No. 21603266 to HS, 21773297 to MY and 21573027 to JL). We thank Prof. Hua Guo for many helpful discussions during the preparation of this article.

References

- 1 F. F. Crim, *Acc. Chem. Res.*, 1999, **32**, 877–884.
- 2 D. C. Clary, *Proc. Natl. Acad. Sci. U. S. A.*, 2008, **105**, 12649–12653.
- 3 S. Yan, Y.-T. Wu and K. Liu, *Proc. Natl. Acad. Sci. U. S. A.*, 2008, **105**, 12667–12672.
- 4 H. Guo and B. Jiang, *Acc. Chem. Res.*, 2014, **47**, 3679–3685.
- 5 H. Guo and K. Liu, *Chem. Sci.*, 2016, **7**, 3992–4003.
- 6 B. Fu, X. Shan, D. H. Zhang and D. C. Clary, *Chem. Soc. Rev.*, 2017, **46**, 7625–7649.
- 7 J. C. Polanyi, *Acc. Chem. Res.*, 1972, **5**, 161–168.
- 8 J. Li, B. Jiang, H. Song, J. Ma, B. Zhao, R. Dawes and H. Guo, *J. Phys. Chem. A*, 2015, **119**, 4667–4687.
- 9 H. Song and H. Guo, *J. Phys. Chem. A*, 2015, **119**, 826–831.
- 10 H. Song, S.-Y. Lee, Y. Lu and H. Guo, *J. Phys. Chem. A*, 2015, **119**, 12224–12230.
- 11 H. Song, M. Yang and H. Guo, *J. Chem. Phys.*, 2016, **145**, 131101.
- 12 H. Song, Y. Lu, J. Li, M. Yang and H. Guo, *J. Chem. Phys.*, 2016, **144**, 164303.
- 13 B. Jiang, M. Yang, D. Xie and H. Guo, *Chem. Soc. Rev.*, 2016, **45**, 3621–3640.
- 14 R. Atkinson, *Chem. Rev.*, 1986, **86**, 69–201.
- 15 A. A. Nanayakkara, G. G. Balintkurti and I. H. Williams, *J. Phys. Chem.*, 1992, **96**, 3662–3669.
- 16 D. W. Arnold, C. Xu and D. M. Neumark, *J. Chem. Phys.*, 1995, **102**, 6088–6099.
- 17 M. K. Dubey, R. Mohrschladt, N. M. Donahue and J. G. Anderson, *J. Phys. Chem. A*, 1997, **101**, 1494–1500.
- 18 M. R. Hand, C. F. Rodriguez, I. H. Williams and G. G. Balint-Kurti, *J. Phys. Chem. A*, 1998, **102**, 5958–5966.
- 19 L. Masgrau, A. Gonzalez-Lafont and J. M. Lluch, *J. Phys. Chem. A*, 1999, **103**, 1044–1053.
- 20 V. S. Langford, A. J. McKinley and T. I. Quickenden, *J. Am. Chem. Soc.*, 2000, **122**, 12859–12863.
- 21 S. Hamad, S. Lago and J. A. Mejias, *J. Phys. Chem. A*, 2002, **106**, 9104–9113.
- 22 I. W. M. Smith and A. R. Ravishankara, *J. Phys. Chem. A*, 2002, **106**, 4798–4807.
- 23 P. Cabral do Couto, R. C. Guedes, B. J. Costa Cabral and J. A. Martinho Simões, *J. Chem. Phys.*, 2003, **119**, 7344–7355.
- 24 M. D. Marshall and M. I. Lester, *J. Phys. Chem. B*, 2005, **109**, 8400–8406.
- 25 B. Wilson, *Chem. Eng. News*, 2005, **83**, 39.
- 26 M. A. Allodi, M. E. Dunn, J. Livada, K. N. Kirschner and G. C. Shields, *J. Phys. Chem. A*, 2006, **110**, 13283–13289.
- 27 D. C. McCabe, B. Rajakumar, P. Marshall, I. W. M. Smith and A. R. Ravishankara, *Phys. Chem. Chem. Phys.*, 2006, **8**, 4563–4574.

- 28 W. J. Cooper, C. J. Cramer, N. H. Martin, S. P. Mezyk, K. E. O'Shea and C. von Sonntag, *Chem. Rev.*, 2009, **109**, 1302–1345.
- 29 E. Codorniu-Hernandez and P. G. Kusalik, *J. Am. Chem. Soc.*, 2012, **134**, 532–538.
- 30 T. Uchimaru, A. K. Chandra, S. Tsuzuki, M. Sugie and A. Sekiya, *J. Comput. Chem.*, 2003, **24**, 1538–1548.
- 31 J. Gonzalez, M. Caballero, A. Aguilar-Mogas, M. Torrent-Sucarrat, R. Crehuet, A. Sole, X. Gimenez, S. Olivella, J. M. Bofill and J. M. Anglada, *Theor. Chem. Acc.*, 2011, **128**, 579–592.
- 32 J.-H. Park, *Asian J. Atmos. Environ.*, 2015, **9**, 158–165.
- 33 M. Bai, D. Lu and J. Li, *Phys. Chem. Chem. Phys.*, 2017, **19**, 17718–17725.
- 34 H. J. Deyerl, A. K. Luong, T. G. Clements and R. E. Continetti, *Faraday Discuss.*, 2000, **115**, 147–160.
- 35 K. S. Kim, H. S. Kim, J. H. Jang, H. S. Kim, B. J. Mhin, Y. Xie and H. F. Schaefer, *J. Chem. Phys.*, 1991, **94**, 2057–2062.
- 36 Y. M. Xie and H. F. Schaefer, *J. Chem. Phys.*, 1993, **98**, 8829–8834.
- 37 P. D. Cooper, H. G. Kjaergaard, V. S. Langford, A. J. McKinley, T. I. Quickenden and D. P. Schofield, *J. Am. Chem. Soc.*, 2003, **125**, 6048–6049.
- 38 A. Engdahl, G. Karlstrom and B. Nelander, *J. Chem. Phys.*, 2003, **118**, 7797–7802.
- 39 D. P. Schofield and H. G. Kjaergaard, *J. Chem. Phys.*, 2004, **120**, 6930–6934.
- 40 Y. Ohshima, K. Sato, Y. Sumiyoshi and Y. Endo, *J. Am. Chem. Soc.*, 2005, **127**, 1108–1109.
- 41 C. S. Brauer, G. Sedo, E. M. Grumstrup, K. R. Leopold, M. D. Marshall and H. O. Leung, *Chem. Phys. Lett.*, 2005, **401**, 420–425.
- 42 S. Du, J. S. Francisco, G. K. Schenter, T. D. Iordanov, B. C. Garrett, M. Dupuis and J. Li, *J. Chem. Phys.*, 2006, **124**, 224318.
- 43 M. A. Allodi, M. E. Dunn, J. Livada, K. N. Kirschner and G. C. Shields, *J. Phys. Chem. A*, 2006, **110**, 13283–13289.
- 44 T. D. Crawford, M. L. Abrams, R. A. King, J. R. Lane, D. P. Schofield and H. G. Kjaergaard, *J. Chem. Phys.*, 2006, **125**, 204302.
- 45 C. S. Brauer, G. Sedo, E. Dahlke, S. Wu, E. M. Grumstrup, K. R. Leopold, M. D. Marshall, H. O. Leung and D. G. Truhlar, *J. Chem. Phys.*, 2008, **129**, 104304.
- 46 D. M. Chipman, *J. Phys. Chem. A*, 2008, **112**, 13372–13381.
- 47 S. Wu, G. Sedo and K. R. Leopold, *J. Mol. Spectrosc.*, 2009, **253**, 35–40.
- 48 K. Tsuji and K. Shibuya, *J. Phys. Chem. A*, 2009, **113**, 9945–9951.
- 49 P. Soloveichik, B. A. O'Donnell, M. I. Lester, J. S. Francisco and A. B. McCoy, *J. Phys. Chem. A*, 2010, **114**, 1529–1538.
- 50 D. M. Chipman, *J. Phys. Chem. A*, 2011, **115**, 1161–1171.
- 51 E.-L. Zins, P. R. Joshi and L. Krim, *Mon. Not. R. Astron. Soc.*, 2012, **426**, 3070–3078.
- 52 E. Galbis, E. Giglio and B. Gervais, *J. Chem. Phys.*, 2013, **139**, 164313.
- 53 G. J. Hoffman, P. K. Gurunathan, J. S. Francisco and L. V. Slipchenko, *J. Chem. Phys.*, 2014, **141**, 104315.
- 54 F. J. Hernandez, J. T. Brice, C. M. Leavitt, T. Liang, P. L. Raston, G. A. Pino and G. E. Douberly, *J. Chem. Phys.*, 2015, **143**, 12.
- 55 A. Gao, G. Li, B. Peng, Y. Xie and H. F. Schaefer, *J. Phys. Chem. A*, 2016, **120**, 10223–10230.
- 56 K. Shao, J. Chen, Z. Zhao and D. H. Zhang, *J. Chem. Phys.*, 2016, **145**, 071101.
- 57 T. B. Adler, G. Knizia and H.-J. Werner, *J. Chem. Phys.*, 2007, **127**, 221106.
- 58 G. Knizia, T. B. Adler and H.-J. Werner, *J. Chem. Phys.*, 2009, **130**, 054104.
- 59 W. L. Hase, R. J. Duchovic, X. Hu, A. Komornicki, K. F. Lim, D.-H. Lu, G. H. Peslherbe, K. N. Swamy, S. R. V. Linde, A. Varandas, H. Wang and R. J. Wolf, *Quantum Chem. Program Exch. Bull.*, 1996, **16**, 671.
- 60 X. Hu, W. L. Hase and T. Pirraglia, *J. Comput. Chem.*, 1991, **12**, 1014–1024.
- 61 H.-J. Werner, P. J. Knowles, G. Knizia, F. R. Manby, M. Schütz and others, *MOLPRO, version 2012.1, a package of ab initio programs*, 2012, see <http://www.molpro.net>.
- 62 G. Rauhut, G. Knizia and H.-J. Werner, *J. Chem. Phys.*, 2009, **130**, 054105.
- 63 D. Feller and K. A. Peterson, *J. Chem. Phys.*, 2013, **139**, 084110.
- 64 G. Czako, I. Szabo and H. Telekes, *J. Phys. Chem. A*, 2014, **118**, 646–654.
- 65 M. J. Frisch, G. W. Trucks, H. B. Schlegel, G. E. Scuseria, M. A. Robb, J. R. Cheeseman, G. Scalmani, V. Barone, G. A. Petersson, H. Nakatsuji, X. M. Li and others, *Gaussian 09, Revision B.01*, Gaussian, Inc., Wallingford CT, 2009.
- 66 B. Jiang and H. Guo, *J. Chem. Phys.*, 2013, **139**, 054112.
- 67 J. Li, B. Jiang and H. Guo, *J. Chem. Phys.*, 2013, **139**, 204103.
- 68 B. Jiang and H. Guo, *J. Chem. Phys.*, 2014, **141**, 034109.
- 69 B. J. Braams and J. M. Bowman, *Int. Rev. Phys. Chem.*, 2009, **28**, 577–606.
- 70 Z. Xie and J. M. Bowman, *J. Chem. Theory Comput.*, 2009, **6**, 26–34.
- 71 M. T. Hagan and M. B. Menhaj, *IEEE Trans. Neural Netw.*, 1994, **5**, 989–993.
- 72 L. M. Raff, R. Komanduri, M. Hagan and S. T. S. Bukkapatnam, *Neural Networks in Chemical Reaction Dynamics*, Oxford University Press, Oxford, 2012.
- 73 Z.-H. Zhou, J. Wu and W. Tang, *Artif. Intell.*, 2002, **137**, 239–263.
- 74 J. Espinosa-García, J. L. Bravo and C. Rangel, *J. Phys. Chem. A*, 2007, **111**, 2761–2771.
- 75 J. Espinosa-García and J. L. Bravo, *J. Phys. Chem. A*, 2008, **112**, 6059–6065.
- 76 J. C. Corchado and J. Espinosa-García, *Phys. Chem. Chem. Phys.*, 2009, **11**, 10157–10164.
- 77 G. Czako and J. M. Bowman, *J. Chem. Phys.*, 2009, **131**, 244302.
- 78 J. Li, J. C. Corchado, J. Espinosa-García and H. Guo, *J. Chem. Phys.*, 2015, **142**, 084314.
- 79 R. J. Duchovic and G. C. Schatz, *J. Chem. Phys.*, 1986, **84**, 2239–2246.
- 80 G. C. Schatz, *Comput. Phys. Commun.*, 1988, **51**, 135–147.
- 81 D. G. Truhlar and J. T. Muckerman, *Atom-Molecule Collision Theory*, ed. R. B. Bernstein, Plenum, New York, 1979.

- 82 L. Bonnet, *Int. Rev. Phys. Chem.*, 2013, **32**, 171–228.
- 83 G. Czako, Y. Wang and J. M. Bowman, *J. Chem. Phys.*, 2011, **135**, 151102.
- 84 G. Czako, *J. Phys. Chem. A*, 2012, **116**, 7467–7473.
- 85 J. Zheng, J. L. Bao, R. Meana-Pañeda, S. Zhang, B. J. Lynch, J. C. Corchado, Y.-Y. Chuang, P. L. Fast, W.-P. Hu, Y.-P. Liu, G. C. Lynch, K. A. Nguyen, C. F. Jackels, A. F. Ramos, B. A. Ellingson, V. S. Melissas, J. Villà, I. Rossi, E. L. Coitiño, J. Pu and T. V. Albu, *POLYRATE, version 9.7*, Department of Chemistry and Supercomputing Institute, University of Minnesota, Minneapolis, Minnesota 55455, 2007.
- 86 H. Guo, *Int. Rev. Phys. Chem.*, 2012, **31**, 1–68.